Available online at www.sciencedirect.com
ScienceDirect
ELSEVIER
Nuclear Instruments and Methods in Physics Research A 565 (2006) 841–854
NUCLEAR INSTRUMENTS & METHODS IN PHYSICS RESEARCH Section A
www.elsevier.com/locate/nima

Integrating Silicon detector with segmentation for scanning transmission X-ray microscopy

Michael Feser[a,1], Benjamin Hornberger[a], Chris Jacobsen[a], Gianluigi De Geronimo[b], Pavel Rehak[b,*], Peter Holl[c,2], Lothar Strüder[d,2]

[a]Department of Physics and Astronomy, Stony Brook University, Stony Brook, NY 11794-3800, USA
[b]Brookhaven National Laboratory, Instrumentation Division, Upton, NY 11973, USA
[c]PNSensor GmbH, Römerstr. 28, 80803 Munich, Germany
[d]MPI für Extraterrestrische Physik, 85741 Garching, Germany

Received 11 April 2006; accepted 10 May 2006
Available online 9 June 2006

Abstract

Scanning transmission X-ray microscopes require detectors with high quantum efficiency and wide dynamic range. While large area detectors provide absorption contrast, the addition of spatial segmentation adds phase contrast imaging capabilities. We describe a charge integrating Silicon detector for use at energies from 200–1000 eV. The detector uses patterned rectifying junctions on high-resistivity n-type Silicon, with separate current readout for each segment. The detector has been subdivided into eight regions arranged in a circular geometry according to the beam profile in a scanning X-ray microscope. The uncooled chip is fully depleted by a positive bias voltage applied at the ohmic contact on the back side. X-rays are collected on the radiation-hard back side with very high efficiency ($>75\%$ for 250 eV X-rays), and compact, low-noise electronics integrate the current from the detector segments. The RMS noise of the combined system is about 500 electrons/channel for a 1 ms integration time, which is equivalent to about five photons per channel at 360 eV X-ray energy.
© 2006 Elsevier B.V. All rights reserved.

PACS: 07.85.Fv; 07.85.Tt; 07.85.Qe

Keywords: X-ray microscopy; X-ray spectromicroscopy; X-ray detectors; X-ray phase contrast imaging

1. Introduction

Considerable cost and effort has gone into the development of high-brightness synchrotron radiation sources, beamlines, and high-resolution focusing optics for X-ray microscopy. However, fewer developments have been reported on detectors specialized for such experiments. In full field transmission X-ray microscopy (TXM), a magnified two-dimensional X-ray image must be recorded over an integration time ranging from tenths to tens of seconds with a detector pixel size of about 20 μm or less; these requirements can be met by commercially available CCD detectors. In scanning transmission X-ray microscopy (STXM; see Fig. 1), a specimen is scanned through a focused X-ray spot, and the image is formed pixel by pixel by collecting the transmitted flux for each scan position, with per-pixel times ranging from tenths to tens of milliseconds in present instruments. This per-pixel dwell time is determined by limitations including the available coherent flux for collecting 10^3–10^4 photons per pixel with low-contrast specimens, and limitations on the speed of scanning the specimen or the X-ray optics. The resulting net count rate of 10^5–10^8 Hz for pulse-counting detectors spans a range where pulse-counting begins to be problematic yet where signal current measurements are difficult. Furthermore, it is often desirable to have some spatial

*Corresponding author. Tel.: +1 631 344 3964.
E-mail addresses: benjamin.hornberger@stonybrook.edu (B. Hornberger), rehak@bnl.gov (P. Rehak).
[1]Current address: Xradia Inc., 4075A Sprig Dr., Concord, CA 94520, USA.
[2]MPI-HLL, Otto-Hahn-Ring 6, 81739 Munich, Germany.

0168-9002/$ - see front matter © 2006 Elsevier B.V. All rights reserved.
doi:10.1016/j.nima.2006.05.086

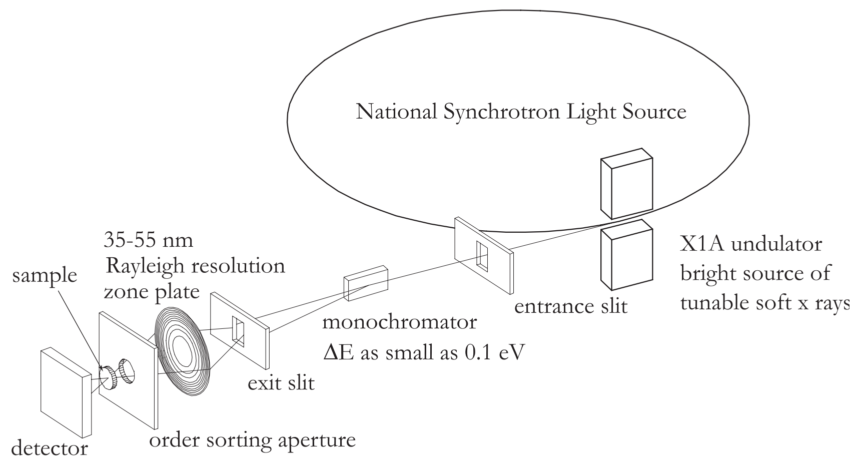

Fig. 1. Schematic of the scanning transmission X-ray microscope [1] at beamline X1A at the National Synchrotron Light Source (Brookhaven National Laboratory). A grating monochromator and a set of slits select a specific X-ray energy (in the range from 250 to 800 eV) and a spatially coherent mode from a high-brightness X-ray source (in this case, a soft X-ray undulator). The combination of a zone plate and an order sorting aperture produces a diffraction limited focus, through which the sample is raster scanned. The X-rays are detected in transmission by a detector.

segmentation of the detector for phase contrast imaging as will be described below. While at present there is no single "out-of-the-box" commercial solution that meets the needs of STXM studies, we describe here a charge-integrating segmented Silicon detector for scanning microscopy experiments that is well suited for present-day signal rates and that provides capabilities for phase contrast imaging.

Detectors used for pulse-counting detection in scanning microscopy have included gas flow proportional counters [1,2], photomultipliers coupled to phosphor screens [3,4], and avalanche photodiodes run in pulse-counting mode [5,6]. Due to detector dead times imposed by space-charge limitations, phosphor lifetime, and/or detection circuitry, these detectors run into non-linearities in their response at count rates of as low as 1 MHz in some cases, or $\gtrsim 10$ MHz in other cases. This presents a limitation to the use of pulse-counting detectors even with present high-brightness synchrotron sources, with greater challenges looming in the future with the development of sources of increasing coherent flux. This suggests the use of current mode for X-ray detection. However, consider the case of the detection of soft X-rays in the energy range of 280–800 eV with absorptive specimens: with Silicon, an electron–hole pair is created per 3.62 eV of ionization energy deposited, so at photon energies of 280 eV as few as about 80 electron–hole pairs will be created. Since strongly absorptive regions of a specimen can reduce the transmitted photon flux to 10^4 Hz or less, this means the current generated in Silicon can range down to 0.2 pA or less, which is difficult to measure as a current with low noise at the kHz bandwidths required for continuous scanning of the specimen. An alternative approach is to use charge integration clocked by the pixel acquisition rate, and that is the approach used by our detector.

A scanning microscope with a large area detector is able to record information only on absorption by the specimen [7], yet phase contrast is significant in many situations in X-ray microscopy and can be used to reduce the radiation dose imparted on the specimen while detecting fine features [8,9]. In full-field imaging systems, phase contrast is often achieved by modifying the phase or intensity distribution of the illumination [10]; the reciprocity principle [11,12] for scanning microscopes allows similar effects to be achieved by modifying the detector response. The ultimate detector might be a fully pixelated detector such as a CCD, and indeed beautiful demonstrations of simultaneous phase and absorption contrast images have been obtained in STXM by using direct X-ray detection in CCD detectors with few-second readout times and a Wigner deconvolution scheme for image analysis [13], or visible light conversion on a phosphor screen followed by imaging on to a fast CCD detector with first-moment analysis of phase contrast [14]. However, these approaches have complications of data rate (even readout times as fast as a millisecond can add significant delay to scans with millisecond pixel dwell times), storage, and signal-to-noise (one is dividing the transmitted signal among 10^3–10^6 pixels, so the noise requirements per pixel become quite demanding). Fortunately, full pixelation of the detector is not required. Since the scanned beam is usually produced by a circular objective lens which is mapped onto the detector in the far-field of the specimen, even a modest number of segments (e.g., a quadrant arrangement with large surrounding annulus) enables the simple implementation of phase [15,16] and dark-field contrast [17,18] in addition to absorption contrast in STXM. (The size of the annulus must be selected with care since it plays a role on image contrast [19]; this is easily set in our detector through the use of optical lithography to define the detector segmentation.) Our detector uses annular quadrants, plus additional segments, to enable phase contrast imaging at millisecond-range dwell times with good signal to noise and a modest data rate.

We describe here the principles of the detector design and readout electronics of this instrument which is in operation in a soft X-ray scanning transmission microscope at the National Synchrotron Light Source at Brookhaven National Laboratory. The detector consists of a patterned Silicon chip with eight segments (Section 2) which is operated at room temperature. The signals from the segments are read out by custom-designed low-noise charge integrating electronics (Section 3), and are provided as analog voltages at each sample position. The detector can be absolutely calibrated in terms of X-ray flux (Section 4) and has a very low dark current of about 1 pA, corresponding to about 10^5 photons per second at 280 eV photon energy. It outperforms currently available counting detectors for STXM in terms of the detective quantum efficiency (DQE) for absorption and phase contrast imaging modes (Appendix A). Images and spectra are shown in Section 5 to illustrate the capabilities of the detector. Additional information about the detector system can be found in [20].

2. Silicon chip with segmentation

An ideal detector for STXM should count the number of photons incident on the surface of each detector segment during the pixel dwell time. The detector described here derives the number of incident photons as a ratio of the total charge produced within the segment by X-rays divided by the mean charge produced by a single X-ray photon (STXM uses monochromatic X-rays). A large DQE requires high sensitivity of the detector to X-rays, and low electronic noise (addressed in Section 3). Moreover, there should be no degradation of any of the detection parameters with time as could be expected by accumulated effects of the radiation.

The detector chip is made out of 300 μm thick n-type high-resistivity (5 kΩ cm) Silicon, commonly used for the detection of charged particles and X-rays. The back side of the detector has a continuous n^+ implant which serves as an ohmic contact. The front side of the detector, shown in Fig. 2, has all segments implanted with low-energy Boron which forms a rectifying p^+n^--junction. To achieve a high DQE, the dead layer on the entrance surface of the detector has to be substantially thinner than the absorption length of X-rays, which is about 0.12 μm at 280 eV and 0.48 μm at 520 eV [21]. The chips were fabricated at the Max Planck Institute Semiconductor Laboratory (MPI-HLL) in Munich, Germany, by the technology used to produce fully depleted pn-Charge Coupled Devices (CCDs) for the X-Ray Multi-Mirror satellite (XMM-Newton) [22]. The fabrication process is a planar technology adapted for detector production. Fig. 3 shows the measured quantum efficiencies for the radiation entering through the rectifying p^+n^--junction. The quantum efficiency for 150 eV photons is 63% and increases almost linearly with energy up to 528 eV where it reaches 95%. Above this energy the efficiency drops to about 90% due to absorption in the

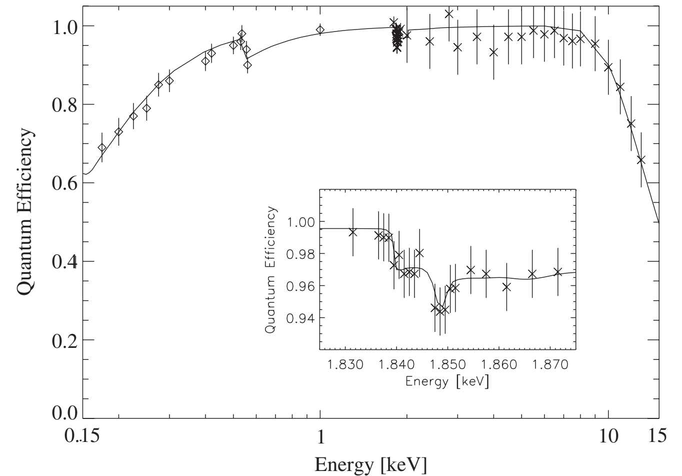

Fig. 3. Quantum efficiency of the pn-detector with a fully depleted thickness of 300 μm [22].

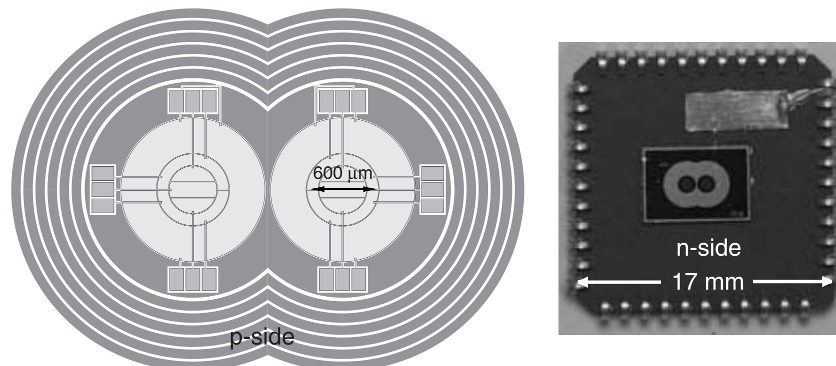

Fig. 2. (Left) Schematic of the front side of the detector. Each chip holds two eight-segment structures (seen in light gray in the center), only one of which is used at a time. One interesting feature of the design is the use of boundaries between individual segments to connect inside segments to their corresponding bonding pads located outside the active area. The large outer segment is a contiguous annulus (the connections to the inner segments are carried across on top of it). (Right) Photograph of the detector chip mounted on a ceramic carrier for back side illumination. One connection can be seen which carries the bias voltage from the upper right pin to the ohmic contact on the chip back side. Underneath the chip (not visible), a cutout is laser-machined into the carrier to allow bonds from the chip front side to the carrier pins.

10 nm thick SiO_2 dead layer on the detector surface. The efficiency then increases with energy and is about 98% above 1 keV, until it drops sharply due to the increased absorption length in Silicon above 8 keV [21].

The readout electronics for the detector (described in detail in Section 3) employs a field effect transistor (FET) preamplifier in a charge integrating configuration. The noise in the electronics is dominated by two main components: parallel noise due to leakage current in the detector and any additional dissipative component connected to the input node of the preamplifier, and series noise related to the input FET in the preamplifier. To keep the parallel noise to a minimum, we stabilized the DC condition of the preamplifier by a reset switch rather than by connecting a high-value resistor to the input. The series noise increases with the capacitance of the detector and its connection. The intrinsic capacitance of the detector is relatively low; each active segment has an area of below 0.2 mm^2, and a classical planer junction Silicon detector of this area and corresponding circumference has the capacitance of only about 1 pF even when the depletion layer extends only 30 μm within the bulk of Silicon. The stray capacitance of the connections is somewhat higher. Because of our desire to rapidly exchange detector chips, we placed the detector chips on ceramic Integrated Circuit (IC) carriers, with the result that the connections from detector segments to the input of their preamplifier each have a capacitance of about 2 pF. We did not consider any more complicated detector structures to further reduce the detector capacitance.

The detector was produced on 300 μm thick Silicon as required by other structures being produced on the same wafer. To collect all charges produced in a few μm under the surface, only a few μm of Silicon have to be depleted of mobile charges. The detector depletes from the rectifying junction inwards. When the radiation is entering the detector from the front side, all charge is collected even from a shallow depletion layer due to the built-in voltage. An additional reverse bias of 1.5 V was applied to improve the electric isolation of the segments. A thin depletion layer corresponds to a smaller active volume generating leakage current. Moreover, the low value of the electric field at the edges of the segments does not require an exceptional quality of the processing of the junction.

The lower leakage current and benefit of a modest bias voltage are the main reasons to operate the detector in front illumination. However, two problems were found in this mode of operation. The first problem was the radiation damage which caused a rapid increase of the leakage current. The second problem was a presence of a spurious signal in all segments when photons were incident on the boundaries between any two segments.

The energy threshold for structural damage of the Silicon lattice by photons is well above 100 keV and can be safely discarded as a reason for radiation damage. The increase of the leakage current as shown in Fig. 4 was most likely due to the buildup of positive charges in the native

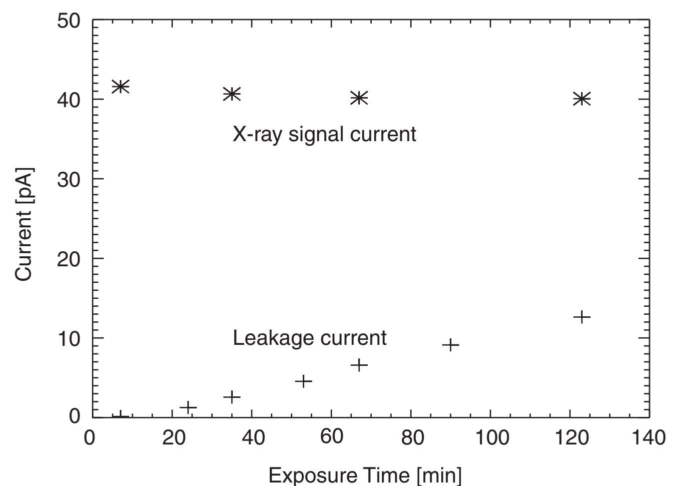

Fig. 4. Radiation damage-induced leakage current increase for one segment.

oxide on the top of the Boron implant. The positive charges in the oxide act as a n-implant, neutralizing the rectifying p^+ implant. When the density of positive charges is high enough, the net junction is not rectifying any more and a large leakage current is injected into the detector. The effect can be more pronounced at the boundaries of the segments where there is an increase of the electric field due to the abrupt end of the implant. This damage could be fully annealed by heating the detector up to about 350 °C for 5 min. We developed a method where the annealing could be done in situ by passing a large current through the detector in a forward direction. The annealing could be done in about 15 min; however, it had to be performed every couple of hours. We have considered such a frequent annealing to be impractical for data taking.

The second problem encountered when the detector was used in front incident mode was the presence of signals in all segments when the radiation was absorbed anywhere in the boundary between segments. It seems that the n-type Silicon under the oxide of the boundary regions is pinched off the main bulk of the n-type Silicon where the depletion voltage is applied. The whole boundary region was thus floating as a single region. The ionization produced anywhere within this region ended up being collected in all segments of the detector.

The above problems with front side illumination have led us to operate the existing detectors in back illumination mode, where photons are incident on the back side which is covered with a continuous shallow ohmic implant. A bias voltage of about +90 V is applied on this contact. The voltage completely depletes the detector of mobile charges, making the whole volume active. When photons are absorbed, electron–hole pairs are produced very close to the ohmic contact. Holes drift across the detector and are collected by individual segments. Sideways diffusion of holes during their drift is small compared to the geometry of the detector, so that the spatial distribution of the X-ray

irradiation pattern is preserved in the electronic signal readout.

No effect of radiation damage was observed during several years of detector operation in back illumination mode. Any positive charges trapped in the oxide right above the ohmic contact make this contact less resistive. Moreover, there is no problem associated with the boundaries between individual segments. Holes drifting toward the boundaries encounter a region of a higher potential, blocking the access to the boundary region. These holes are collected by one of the segments with no signal induced in other segments. To facilitate the alignment of the back side of the detector, the boundaries of the segment are shown by narrow lines of aluminum on the back side of the detector.

The disadvantage of a fully depleted detector is increased parallel noise, because the larger active volume leads to a significant increase of the leakage current. The leakage current from individual segments when detector is biased to 1.5 V are typically about 0.4 pA. The charge collected in 2.5 ms of integration time due to this leakage current is 1 fC or 6200 electron charges. Since the Poissonian fluctuations of 6200 electrons are characterized by a root variance of only 80 electrons, this parallel noise component is well below the required value for the total readout noise of 500 electrons rms. The typical leakage current of a segment when the detector is fully depleted under a bias of 90 V is 2 pA, which represents an increase by a factor of 5 compared to the value above. The parallel noise due to this value of the leakage current is below 200 electrons, still an acceptable value.

At this point we would like to point out that for our kind of readout, where the number of measured photons is derived from the total integrated charge, the actual limit of the tolerable leakage current may not be imposed by the increase of the noise with the square root of the current but by a more practical limit of a given dynamic range of the system. Let us consider a leakage current of 5 pA and a pixel dwell time of 10 ms as might be required in low-signal situations. The parallel noise due to the fluctuation of the charge accumulated by leakage current is 560 electrons, an almost acceptable value. The feedback capacitance of the preamplifier is about 50 fF for the high-gain channels. To accommodate the charge of 50 fC due to the leakage current the output of the preamplifier has to change by 1 V which is a considerable part of its dynamic range. The stages following the preamplifier usually saturate before the preamplifier and we may be left with little dynamic range for the signal.

Based on the above experience, improved detector chips have been fabricated at the Max Planck Semiconductor Lab. The native oxide is removed from the top of the rectifying junctions and replaced with a very thin layer of aluminum. The elimination of the oxide layer should avoid the charging effect and result in substantively improved radiation hardness. The new design also features one new dedicated connection to the previously floating boundary region to remove any charge produced by X-rays and therefore avoid charge injection into the detector segments.

3. Charge integrating electronics

Each of the sensitive segments of the detector chip described above is connected to one of 10 integrating readout channels. The expected soft X-ray signal per 1 ms integration cycle per segment is on the order of 10^5 electrons; in order to be smaller than the noise due to X-ray counting statistics, the electronics noise should be kept below $\sqrt{10^5}$ (about 300 electrons). This requirement means that great care has to be taken in the design of the integrating electronics and the selection of components. In addition, space constraints in the microscope dictate the use of compact components.

Fig. 5 shows a simplified schematic of one channel. It is composed of a charge preamplifier (front-end amplifier (FEA), feedback capacitor C_F and reset switch S1), followed by two parallel RC low-pass filters feeding the two inputs of an instrumentation amplifier (IA). The upper path implements a switch S2 between R and C. The output of the IA goes to a sample-and-hold (SH) circuit with a controlled switch S3.

At the beginning of each integration cycle ($t = 0$), the switches S1 and S2 are closed to the reset position, discharging the feedback capacitor and bringing the output of the IA to zero. At time $t = T_{reset}$ the reset switch S1 opens and the preamplifier is in the configuration to provide low-noise integration of the input charge. The preamplifier output equals the total charge injected at its input for $t > T_{reset}$ divided by the feedback capacitor C_F. At time $t = T_{m1}$ the sampling switch S2 opens, storing the FEA output (filtered with time constant RC) on the capacitor C at the non-inverting input node of IA. The FEA output, identically filtered through the lower RC integrator, drives the inverting input of the IA. The IA output tracks the difference between the two input voltages, thus providing a measurement of the charge integrated onto C_F since the opening of S2. At the end of the integration cycle ($t = T_{m2}$) the sample switch S3 opens, storing the IA output on the SH capacitor for readout. At the same time, a new integration cycle can start. S3 will close once the output has been read by an analog-to-digital converter (ADC), following the next integration cycle. The effective charge integration time is $T_{m2} - T_{m1}$, while the duration of the full cycle is longer due to the reset time. The reset time is set by the pulse width of S2 and must be longer than the settling times, which were empirically determined to be 60 μs for this setup.

3.1. Charge preamplifier

Two critical aspects of the front-end design were the choice of the FEA and the choice and architecture of the reset switch S1. The stringent requirement on the input bias current and the limitation in space led to the choice of a

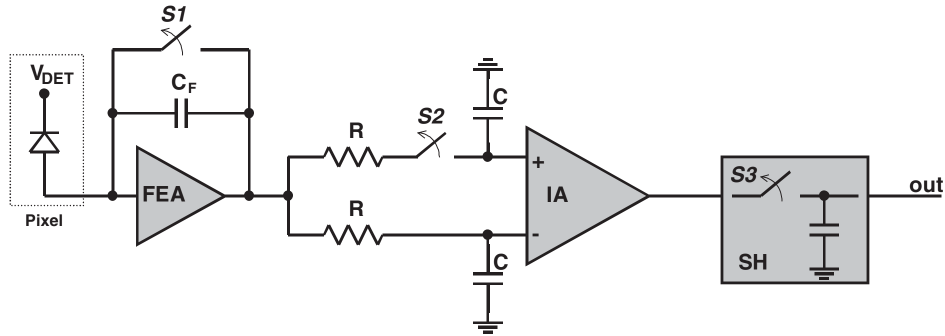

Fig. 5. Simplified schematic of the charge integrating electronics.

Motorola MC33502 as the FEA. This dual amplifier is characterized by (data sheet typical) 40 fA input current, $30 \times 10^3/f + 0.9 \times 10^3\,\mathrm{nV^2/Hz}$ equivalent input noise voltage, 2 pF input capacitance, 100 dB DC voltage gain, and 5 MHz gain bandwidth product. The minimization of the switch leakage current while in the off state suggested the use of the transistor SST4117. This n-channel JFET is characterized by (data sheet typical) 200 fA drain cutoff current, −1.2 V pinch-off voltage, 1.2 pF input capacitance, and 0.3 pF reverse transfer capacitance. In order to minimize both the cutoff current and the impact of the parasitic drain-to-source capacitance (about 240 fF were measured, to be compared to $C_F \simeq 50$ and 200 fF for two different circuits), the dual FET switch approach [23] was adopted, as shown in Fig. 6.

Both J1 and J2 are SST4117 JFETs and are controlled by the same gate voltage V_{GATE1}. When V_{GATE1} is in the high state (about −0.5 V), the switches are closed, exhibiting a resistance $r_{\mathrm{on}} \simeq 200\,\mathrm{k\Omega}$ and a drain saturation current $I_{\mathrm{dsat}} \simeq 20\,\mu\mathrm{A}$. When V_{GATE1} is in the low state (about −1.7 V) the switches are open exhibiting a measured drain leakage current in the sub-50 fA range. The resistor R_F serves the purpose of keeping the node S grounded once the switch is in the open state. The value for R_F must be chosen in order to guarantee a fast and damped reset. The stability can be analyzed evaluating the loop gain from the schematic of Fig. 6. Assuming $R_F \ll r_{\mathrm{on}}$, the loop gain G_{loop} can be approximated as

$$G_{\mathrm{loop}} \simeq \frac{R_F}{r_{\mathrm{on}} + R_F} \frac{A_0}{(1 + sC_i r_{\mathrm{on}})(1 + s\tau_a)} \quad (1)$$

where A_0 and τ_a are, respectively, the DC voltage gain and dominant time constant of the amplifier, C_i is the total capacitance at the input, and s is the Laplace variable. From the equation $1 + G_{\mathrm{loop}} = 0$ it is possible to calculate the damping factor ζ [24]:

$$\zeta \simeq \frac{1}{2}\sqrt{\frac{(C_i r_{\mathrm{on}} + \tau_a)^2}{C_i r_{\mathrm{on}} \tau_a A_0 R_F/(r_{\mathrm{on}} + R_F)}}. \quad (2)$$

In our case $C_i \simeq 5\,\mathrm{pF}$ and a value $R_F = 10\,\mathrm{k\Omega}$ was chosen, leading to $\zeta \simeq 0.4$ (about $\pi/3$ phase margin). This corresponds to an underdamped response with about 3 μs settling time. It must be observed that a further reduction in the value of R_F in order to increase the value of ζ would lead to reduced overshoot but increased settling time, which is a consequence of the reduced loop gain.

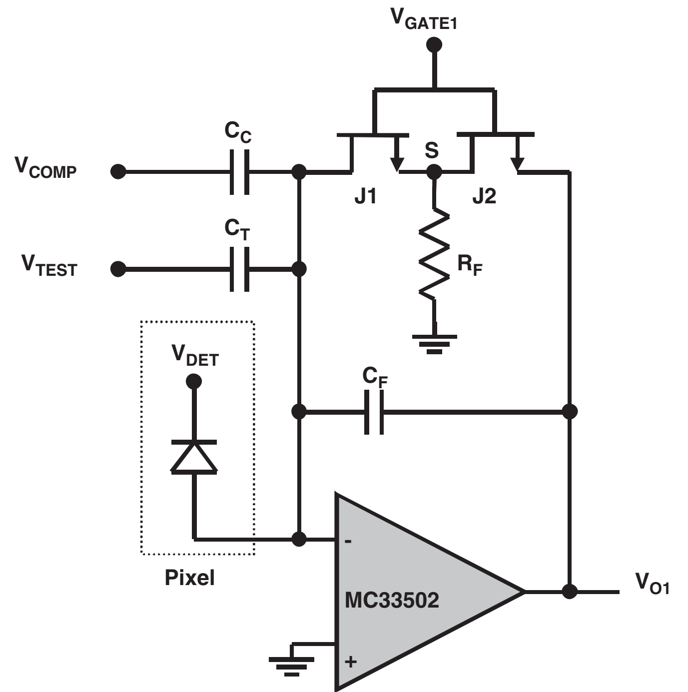

Fig. 6. Schematic of the charge preamplifier with details on the reset switch. The detector element is depicted as a diode.

During the reset of the preamplifier, a feedthrough (i.e., transmission of signal through capacitive coupling) of V_{GATE1} to the preamplifier input via the gate-to-drain capacitance of J1 occurs. This feedthrough may be high enough to bring the preamplifier output to positive saturation. To limit this effect, an inverted pulse V_{COMP} producing an opposite feedthrough via the capacitor C_C (about 500 fF, low dielectric loss, surface mounting) was added and calibrated to produce a net feedthrough so that the output settled at $V_{\mathrm{O1}} \simeq 3\,\mathrm{V}$ at the end of each reset phase (opening of S1). During integration, the output voltage decreases linearly with the charge collected. For calibration and test purposes, a capacitor C_T was also added.

The preamplification channels are assembled on the bottom side of a Teflon board while the detector is mounted on the top side (see Fig. 7). A socket for semiconductor packaging accepts a ceramic carrier onto which the detector chip is glued for quick replacement of the chip. Extension boards are used to bring the preamplifier output signals to the main board containing the remaining multi-channel processing electronics, thus satisfying the geometrical constraints of the existing X-ray microscope.

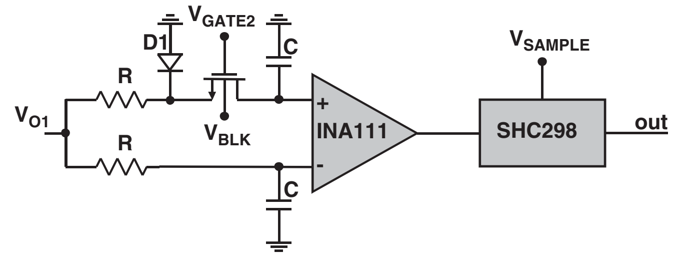

Fig. 8. Schematic of the sampling electronics following the preamplifier.

3.2. Sampling electronics

The charge preamplifier described above delivers a voltage proportional to the charge collected from a detector segment, which is in turn proportional to the number of incident photons. However, this output voltage does not remain steady over a long time period, since the preamplifier must be reset for the next integration interval. As a result, a SH circuit (Fig. 8) is used to capture the voltage output and hold it steady so that it can be read by an ADC (in our case, a National Instruments PCI-6052E board with 16 analog input channels that can be digitized to 16 bits precision at a rate of 333 kS/s).

Because the sampled signal should be held steady during the time when the multi-function board is sequentially digitizing analog voltages on multiple inputs, a low-pass filter is provided on the analog output. This is done by using the RC filters shown in Figs. 5 and 8 with $R = 5\,\mathrm{k}\Omega$ and $C = 1\,\mathrm{nF}$ (see Section 3.4 for the criteria used to determine the time constant RC). The capacitor dielectric material polypropylene was chosen to minimize the dielectric absorption (charge backup) effect [23]. A 0.32% charge backup after several minutes was measured for polypropylene, compared with 2.25% for mica and 1.68% for ceramic materials. Teflon material, characterized by an even lower charge back up effect, was rejected due to much higher cost compared to polypropylene.

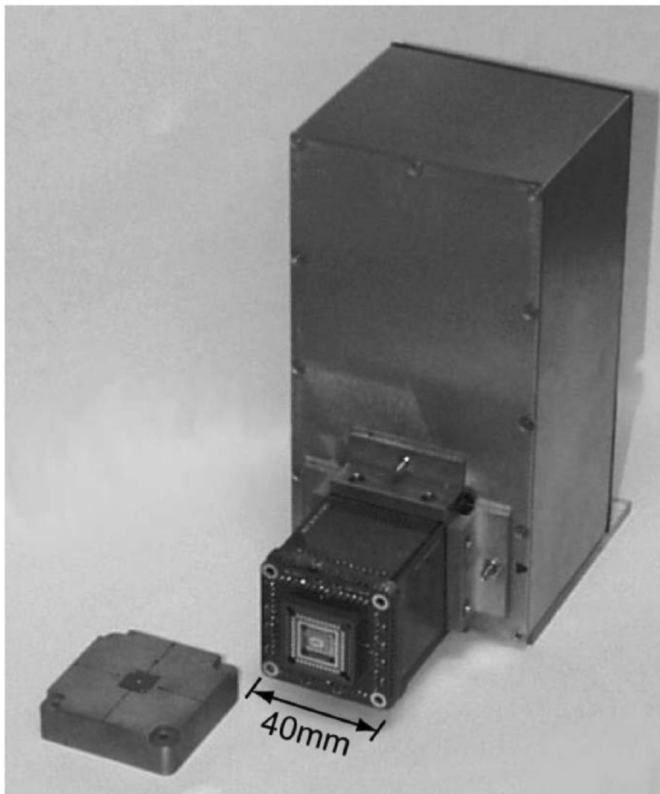

Fig. 7. Photograph of assembled electronics.

The switch S2, which controls holding of the analog voltage, was realized by using the readily available n-channel enhancement-mode MOSFET SD214DE. The bulk was biased at $V_{\mathrm{BLK}} \simeq -1.5\,\mathrm{V}$ while the gate was driven with $V_{\mathrm{GATE2}} \simeq 0$–$5.4\,\mathrm{V}$. During the integration in presence of large amounts of charge, the preamplifier output V_{O1} (and the source of M1) could reach values negative enough to open the channel of M1 (i.e., close the switch S2), thus bringing the output of the differential amplifier back to zero. In order to avoid this unpleasant effect and to provide a defined saturation value, a Schottky diode 1N4148 was added as D1 in Fig. 8. The diode clamps the negative value to $-0.4\,\mathrm{V}$ and thus prevents the opening of M1. A FET-input INA111 was selected for the IA, and set to provide a differential gain 3. A Burr-Brown SHC298 was used to provide the final SH of the signal.

Fig. 9 shows the PSpice simulation of a full 1 ms cycle for the case $C_{\mathrm{F}} = 200\,\mathrm{fF}$. In this simulation, a 100 fC positive charge (corresponding to 625 000 electrons generated in the detector) is injected at the input node 50 μs after the opening of S2, while a 2.5 pA detector leakage current is flowing to the FEA. The cycle starts at $t = 1\,\mathrm{ms}$, when both the switches S1 (V_{GATE1} and V_{COMP} in Fig. 9a) and S2 (V_{GATE2} in Fig. 9b) close. The preamplifier output resets to 0 V with a settling time on the order of 3 μs (detail in Fig. 9e). After a time $T_{\mathrm{reset}} = 10\,\mu\mathrm{s}$ ($t = 1.01\,\mathrm{ms}$), the switch S1 opens (the compensation pulse V_{COMP} is also applied) and the preamplifier output rises to about 3 V (Fig. 9c). The measurement starts after $T_{\mathrm{m1}} = 50\,\mu\mathrm{s}$ ($t = 1.05\,\mathrm{ms}$) with the opening of S2 (V_{GATE2} in Fig. 9b); some perturbation can be observed in Fig. 9c. At time $t = 1.1\,\mathrm{ms}$, a 100 fC charge is injected and the corresponding step can be observed at the inverting input and at the output of IA (Figs. 9d and f, respectively). During the remaining measurement time the effect of the 2.5 pA detector leakage

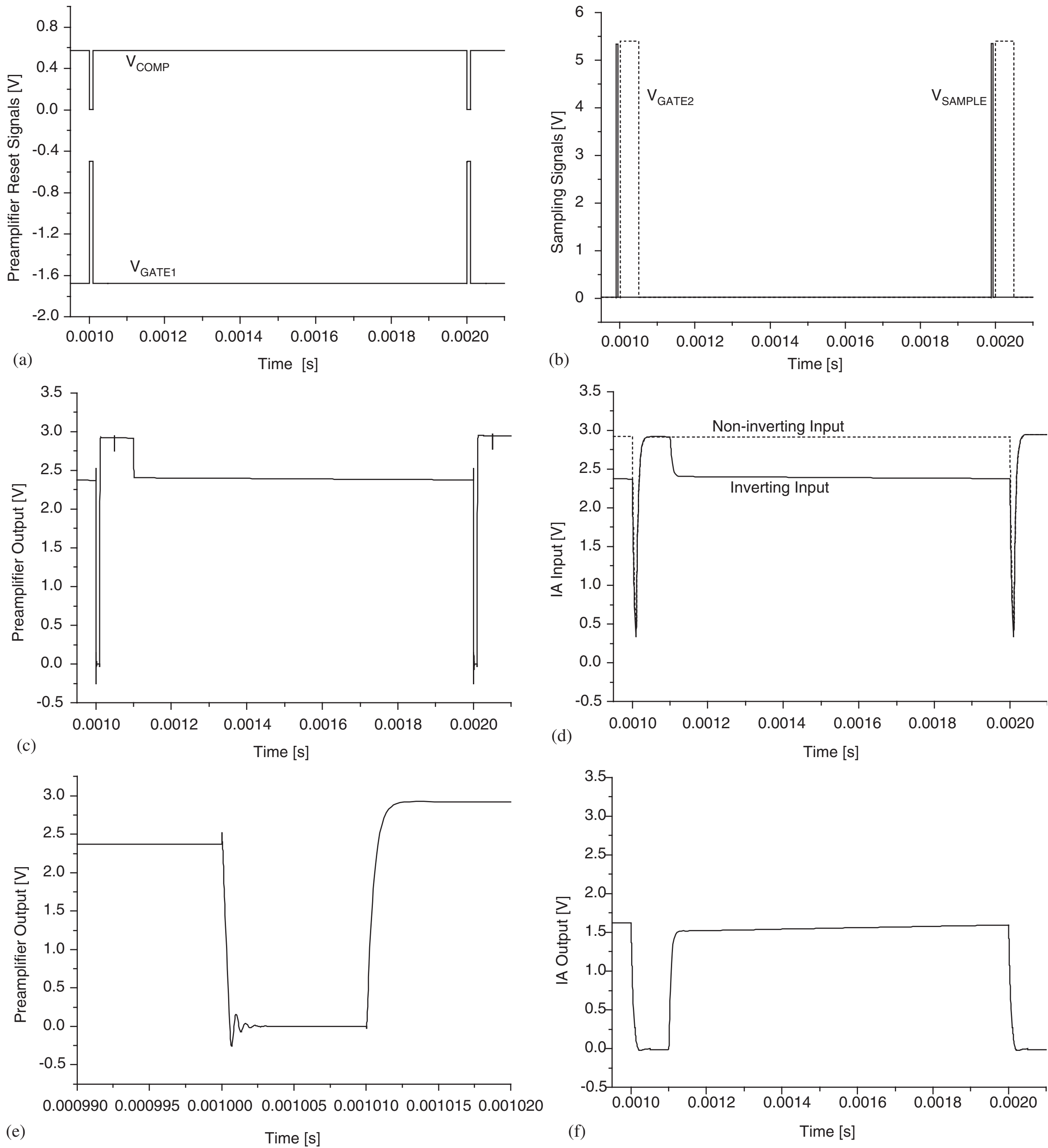

Fig. 9. PSpice simulation results for a full 1 ms cycle for the case $C_F = 200$ fF: (a) preamplifier reset signals; (b) sampling signals; (c) preamplifier output; (d) instrumentation amplifier input; (e) preamplifier output details of reset; (f) instrumentation amplifier output.

current can be observed as a slope both at the inverting input and at the output of IA. After $T_{m2} = 0.99$ ms ($t = 1.99$ ms) the switch S3 is closed, and the measurement is sampled (sampling time is negligible). The overall cycle lasts 1 ms with an effective integration time 0.94 ms.

3.3. Power supply filtering

A last critical aspect of the design was the filtering of the power supplies. Due to the long measurement time, any disturbance from the supply down to a frequency of a few Hz (with particular reference to the 60 Hz and harmonics) could affect the resolution of the system. The relatively high power dissipated by the electronics (about 1.3 W for 10 channels) made the use of a power supply based on batteries unpractical, requiring too frequent calibrations to compensate for the continuous battery discharge.

Low-noise voltage supplies followed by suitably designed active filters with low-pass frequency on the order of 0.016 Hz were adopted, with a dedicated circuit for each of

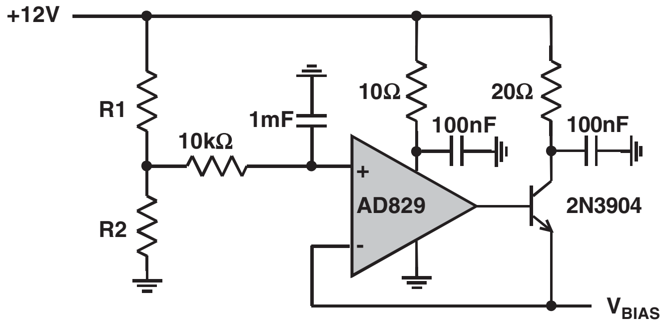

Fig. 10. Detailed schematic of the active filter for the positive supply voltage.

the processing stages. In Fig. 10, a detailed schematic of the active filter for the case of positive supply is shown. The resistive divider $R1/R2$ was adjusted to set the desired voltage. The corresponding case of negative supply is straightforward.

3.4. Resolution and dynamic range

The resolution of the system, which provides filtering with a time constant $\tau_F = RC$ and correlated samplings at times T_{m1} (when S2 in Fig. 5 opens) and T_{m2} (when S3 in Fig. 5 opens), can be expressed in terms of Equivalent Noise Charge (ENC) as [25–27]

$$\mathrm{ENC}^2 \simeq \frac{1}{2}\int_{-\infty}^{T_{m2}} S_{iw} w_{iw}^2(t) + A_{if} w_{if}^2(t) + C_i^2 (S_{vw} w_{vw}^2(t) + A_{vf} w_{vf}^2(t))\,\mathrm{d}t \quad (3)$$

where $A_{if}/f + S_{iw}$ is the noise power spectral density associated with the equivalent parallel input noise generator, $A_{vf}/f + S_{vw}$ is the noise power spectral density associated with the equivalent series input noise generator, C_i is the total input capacitance and $w_{iw}(t)$, $w_{if}(t)$, $w_{vw}(t)$, $w_{vf}(t)$ are the corresponding noise weighting functions, which are, in general, also functions of τ_F, T_{m1}, and T_{m2}. The factor $\frac{1}{2}$ takes into account the assumption that the power spectral densities are unilateral.

The dominant source of parallel input noise is the white shot noise associated with the input leakage current, characterized by the power spectrum $S_{iw} = 2q(I_{leak} + I_{det})$, where I_{leak} is the amplifier plus switch leakage current (absolute values) and I_{det} is the detector leakage current (absolute value), while the $1/f$ component is assumed negligible. The dominant source of series input noise is the noise associated with the FEA, characterized by the power spectrum $S_{vw} = 30 \times 10^3/f + 0.9 \times 10^3\,\mathrm{nV^2/Hz}$ (data sheet typical for MC33502). The total input capacitance is on the order of 5 pF.

The noise weighting functions can be evaluated by considering the weight at time T_{m2} of each impulse occurring at $t < T_{m2}$. If $h(t)$ is the pulse response of the preamplifier/filter, the corresponding noise weighting function is given by

$$w(t) = h(T_{m2} - t) - h(T_{m1} - t)\Phi(T_{m1} - t) \quad (4)$$

where $\Phi(t)$ is the step function at $t = 0$.

The response $h_{iw}(t)$ to a current impulse (such as a white noise current pulse) is given by

$$h_{iw}(t) = \left[1 - \exp\left(-\frac{t}{\tau_F}\right)\right]\Phi(t). \quad (5)$$

The response $h_{vw}(t)$ to a voltage impulse (such as a white noise voltage pulse) is given by

$$h_{vw}(t) = \frac{\mathrm{d}}{\mathrm{d}t} h_{iw}(t) = -\frac{1}{\tau_F}\exp\left(-\frac{t}{\tau_F}\right)\Phi(t). \quad (6)$$

Concerning the weighting functions for the current and voltage $1/f$ noise contributions, the current and voltage $1/f$ noise source contributions can be represented as a superposition of $\Phi(t)\sqrt{2/t}$ pulses randomly arriving at an average rate $A_f/2$ (see [25,28–30] and Appendix A). This gives pulse responses to be used in Eq. (3) of

$$h_{if}(t) = \int_0^t \sqrt{\frac{2}{\tau}} h_{iw}(t - \tau)\,\mathrm{d}\tau \quad (7)$$

and

$$h_{vf}(t) = \int_0^t \sqrt{\frac{2}{\tau}} h_{vw}(t - \tau)\,\mathrm{d}\tau. \quad (8)$$

In Fig. 11, the normalized weighting functions are shown for $\tau_F = 5\,\mu s$, $T_{m1} = 40\,\mu s$, and $T_{m2} = 1\,\mathrm{ms}$.

After algebraic and numerical calculations, the ENC can be approximated by

$$\mathrm{ENC}^2 \simeq S_{iw}(T_{m2} - T_{m1}) + \frac{C_i^2}{\tau_F}\cdot S_{vw} + 23.4\cdot C_i^2 \cdot A_{vf} + 7.5 \cdot A_{if}(T_{m2} - T_{m1})^2. \quad (9)$$

The first two components are the dominant ones (the third component contributes with about 19 rms electrons while the fourth component is negligible). In Fig. 12, the

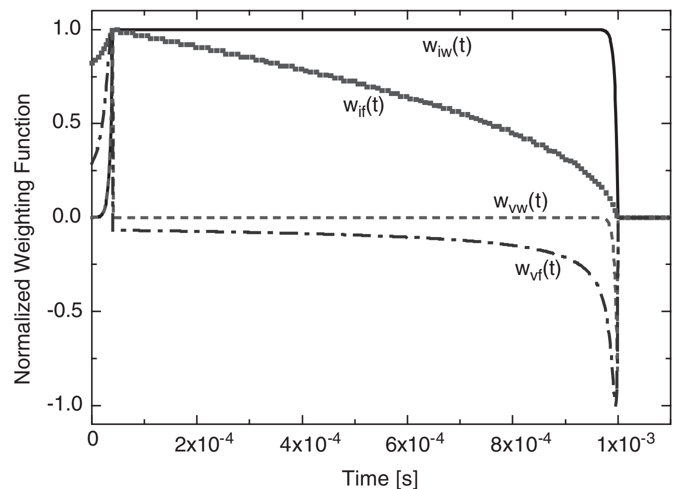

Fig. 11. Normalized weighting functions for $\tau_F = 5\,\mu s$, $T_{m1} = 40\,\mu s$, $T_{m2} = 1\,\mathrm{ms}$.

expected ENC (along with the two dominant components) is compared to the typical measured ENC; this is done for the absence of I_{det} as function of the effective integration time ($T_{m2} - T_{m1}$), and for representative parameter values ($C_i = 5\,pF$, $I_{leak} = 100\,fA$, $\tau_F = 5\,\mu s$). The fitting of the experimental data shows that the S_{vw} was about 2.2 times higher than the data sheet typical (i.e., about $10^3\,nV^2/Hz$), while the extracted detector leakage current was $I_{det} \simeq 300\,fA$ (assuming negligible surface leakage on the front-end assembly). It must be observed that the noise associated with the reset switch activity (also known as kTC_f noise), as well as any feedthrough or charge injection occurring during the reset, do not contribute because it is subtracted by the sampling electronics.

The voltage excursion available at the output of the preamplifier is on the order of 4 V, starting from about +3 V as in Fig. 9c and ending at about −1 V. The upper limit is set by the threshold voltage of M1 in Fig. 8, while the lower limit is set by the negative supply of the FEA. The maximum charge per integrating time is consequently given by

$$Q_{max} \simeq C_F[4\,V - (I_{leak} + I_{det})T_{m2}] \tag{10}$$

and it is determined by the value of the feedback capacitor ($C_F \simeq 50$ and 200 fF for two different circuits) and by the net leakage current $I_{leak} + I_{det}$. The dynamic range is given by

$$\mathrm{DR} = \frac{Q_{max}}{\mathrm{ENC}} \simeq \frac{C_F[4\,V - (I_{leak} + I_{det})(T_{m2} - T_{m1})]}{\sqrt{q(I_{leak} + I_{det})(T_{m2} - T_{m1}) + (C_i^2/\tau_F)S_{vw}}} \tag{11}$$

which is on the order of 65–80 dB.

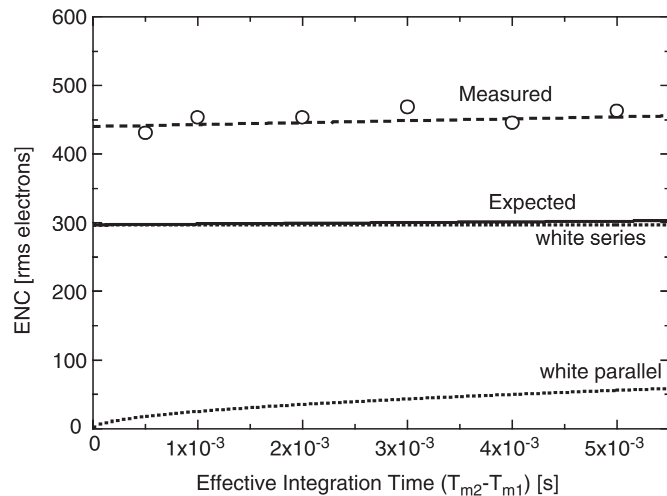

Fig. 12. Expected equivalent noise charge (ENC) for $C_i = 5\,pF$, $I_{leak} = 100\,fA$, $\tau_F = 5\,\mu s$ in absence of I_{det} along with its two dominant components, compared to the typical measured ENC.

4. Calibration and measurements

The detector system has been characterized both using test signals injected into the capacitor C_T (see Fig. 6), and X-ray illumination in a STXM. These tests have provided information on calibration of the detector and its measured performance.

4.1. Correction of channel crosstalk

We have observed varying crosstalk between detector channels, which has been identified as being due to capacitive coupling of the FEA output to the input node of other preamplifiers. Introduction of an additional shield at ground potential (mounted directly on top of the front-end printed circuit board holding the preamplifiers) reduced this effect significantly. The remaining coupling is small (less than 0.2% from adjacent channels). The coupling coefficients have been measured, giving a correction that can be applied after data acquisition. The coupling depends only on the physical parameters such as the geometry and layout of the printed circuit and therefore does not change with time. It does not have a significant impact on the dark noise figure of a corrected channel, since the coupling is very small.

4.2. Detector calibration

Having removed the interdependence of channels, it is sufficient to describe the calibration procedure for one channel. The switches S1, S2 and S3 which manage the integration cycle of the detector are externally controlled by a commercially available timing module (Quantum Composers, PO Box 4248, Bozeman, MT 59772; model PG9514 option 403). At the beginning of an integration cycle, the X-ray microscope control electronics provide a trigger signal from which the switch signals for the detector are generated. The time between trigger signals can vary from scan to scan, which necessitates normalizing the signal to the effective integration time $T_{int} = T_{m2} - T_{m1}$. T_{int} is measured independently from a clock signal by the microscope electronics. The output voltage of the SH circuit U_{SH} is digitized by a 16-bit multi-channel ADC and can be written as

$$U_{SH} = U_0 + \alpha(I_{dark} + I_{signal})T_{int} \tag{12}$$

where α is a calibration constant and U_0 is a time-independent integration pedestal. The current I_{signal} is the current generated by X-rays, while $I_{dark} = I_{det} + I_{leak}$ represents the dark current (without X-rays) of the detector plus any parasitic leakage currents. If the average charge deposited in the detector per incident X-ray photon is q, the signal current is related to the photon flux Φ as $I_{signal} = q\Phi$, resulting in

$$\Phi = \frac{U_{SH} - U_0 - \alpha I_{dark}T_{int}}{\alpha q T_{int}}. \tag{13}$$

The parameter q contains the photon detection efficiency of the detector and the statistics of photon conversion to electron–hole pairs in the Silicon; therefore depends on the X-ray energy. Once the parameters U_0, α, I_{dark} and q are known, Eq. (13) can be used to calculate the incident photon flux.

4.3. Determination of calibration parameters

The integration time T_{int} differs from the time between samples by the system reset time (dead time), during which no integration takes place. The length of the reset time (width of the S2 pulse) is currently limited to values above $60\,\mu s$ due to instabilities in the reset of the feedback capacitor. A conservative setting of $100\,\mu s$ has been chosen at present, since integration times are $\gtrsim 1\,ms$. For future experiments at higher brightness sources requiring very short integration times, the reset circuit has to be improved.

The calibration constant α is determined by measuring the increase of U_{SH} for a known input charge on the FEA input node. This is accomplished by applying a step voltage to the test capacitor C_{T} with previously measured capacitance. Since the relative accuracy of this value between channels is more important than the absolute value, the response to a constant-intensity X-ray beam is measured and the α values are adjusted to yield the same response on all channels. In the current implementation, the detector has five high-sensitivity channels with $\alpha \simeq 50\,\mathrm{mV/fC}$ and five low-sensitivity channels with $\alpha \simeq 10\,\mathrm{mV/fC}$. To reduce α, a capacitor can be added in parallel to the existing feedback capacitance.

The voltage offset U_0 and the dark current I_{dark} are determined by a linear fit to U_{SH} for varying integration times with the detector running in dark conditions (no X-rays incident). The average charge deposited per X-ray q is not readily accessible for measurement. The parameter q can be written as

$$q = \varepsilon \frac{E[\mathrm{eV}]}{3.62} \cdot e \tag{14}$$

where ε is the X-ray detection efficiency (see Fig. 3) and e the charge of the electron.

4.4. Verification of detector efficiency

For a properly calibrated detector, Eq. (13) can be used to verify that the calculated detector efficiency ε is correct. For this purpose, the incident X-ray flux Φ is measured independently with a photodiode for which an absolute calibration is available [31,32]. A measurement beam was generated by aperturing a collimated 520 eV X-ray beam to $10\,\mu m$ diameter. The reference photodiode delivered a current of $(350 \pm 20)\,\mathrm{pA}$, corresponding to a photon flux of $(20.1 \pm 1.1)\,\mathrm{MHz}$. The integrating Silicon detector indicated a photon flux of $(18.8 \pm 0.4)\,\mathrm{MHz}$ for the measurement beam (not taking into account the factor ε in Eq. (14)). The ratio of these two fluxes gives a measured detective quantum efficiency of $\mathrm{DQE} = (93.5 \pm 5.5)\%$, which is in very good agreement with the expected result of about 91% shown in Fig. 3. One potential source of error in this measurement is the temporal instability of the measurement beam on a timescale of minutes. Since the reference photodiode flux measurement accounts for the transmission of its 150 nm thick aluminum coating (this layer is present to minimize sensitivity to visible light), errors in the assumption of the aluminum layer's thickness and density can also affect the DQE measurement. Using values for the bulk density of aluminum, and tabulated data of X-ray absorption coefficients [21], the transmission of this aluminum layer is expected to be 0.76 at 520 eV photon energy.

4.5. Measurements

During the calibration procedure, the dark signal (no X-rays incident) is measured for several dwell times. A linear fit to the voltage versus dwell time yields the offset U_0 and the product $\alpha \times I_{\mathrm{dark}}$ (Fig. 13a). The voltage output is the average of a whole "image" collected with a fixed dwell time. A histogram of the voltages from one image (Fig. 13b) allows an estimate of the noise by performing a Gaussian fit to the distribution. The dependency of the noise on the dwell time is shown in Fig. 13c. Finally, the power spectrum of voltage samples obtained in constant time intervals allows to identify noise pickup at particular frequency. In the ideal case, a white (flat) power spectrum would be expected. As can be seen from Fig. 13d, almost no frequency pickup can be observed.

5. Results and conclusions

The detector has been in routine use at one of the STXMs at beamline X1A at the National Synchrotron Light Source since 2002, giving excellent performance in spectromicroscopy experiments. Fig. 14 shows an example each of a differential phase contrast (DPC) image and a spectrum obtained. With further efforts in data analysis, Fourier filtering [33,34] provides a means for quantitative reconstruction of the complex specimen function (absorption *and* phase shift).

As absorption contrast in low-Z elements decreases with increasing X-ray energy while phase contrast remains quite strong [8], phase contrast capabilities become even more important for instruments operating in the multi-keV region. The detector described here was built for soft X-ray applications at a second generation synchrotron source. A new set of electronics is currently under development to accommodate the much higher signal currents present at microprobes operating in the multi-keV region at a third generation synchrotron like the

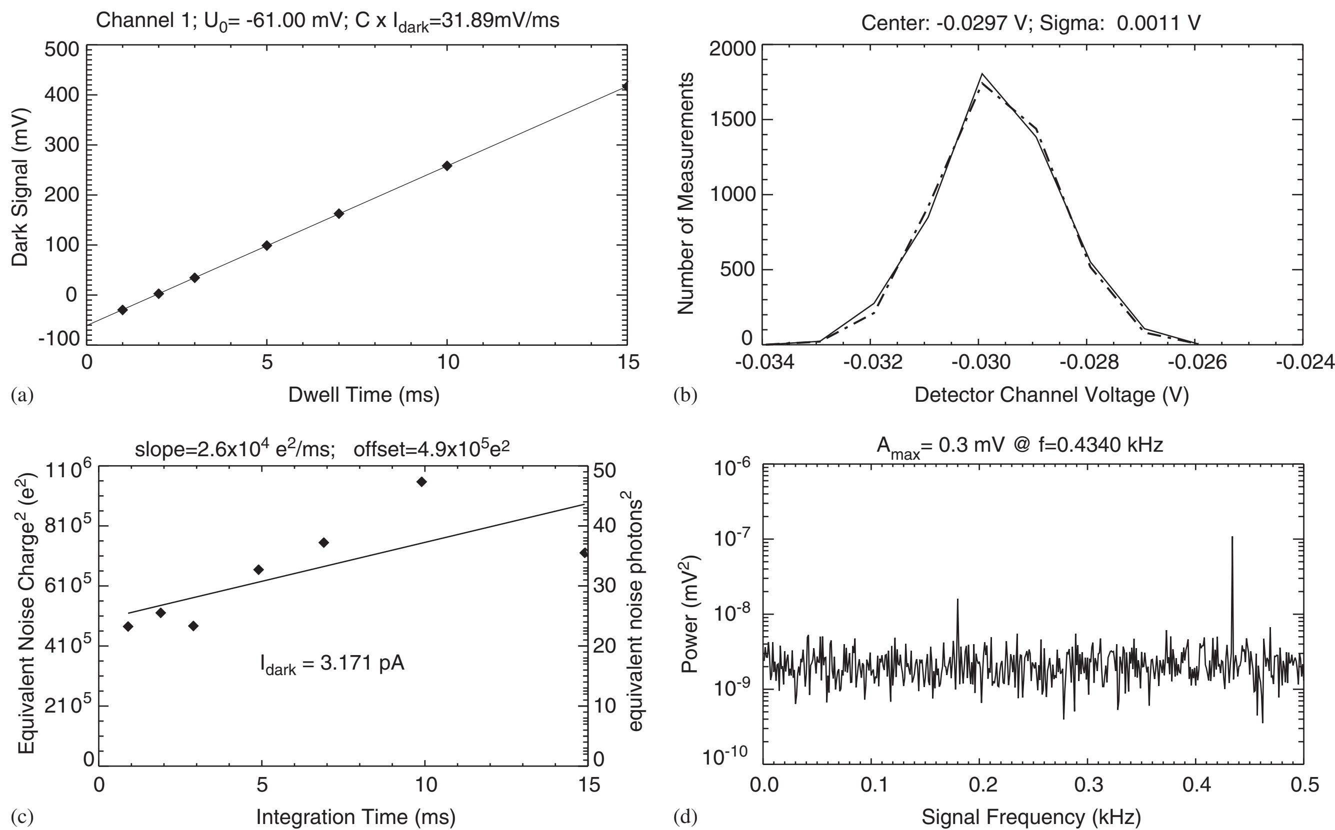

Fig. 13. Measurements of the dark signal obtained during the calibration process for one detector channel: (a) dark signal versus dwell time; (b) histogram (solid line) and Gaussian fit (dashed line) of measurements; (c) noise versus integration time; (d) power spectrum obtained by Fourier transform of consecutive samples.

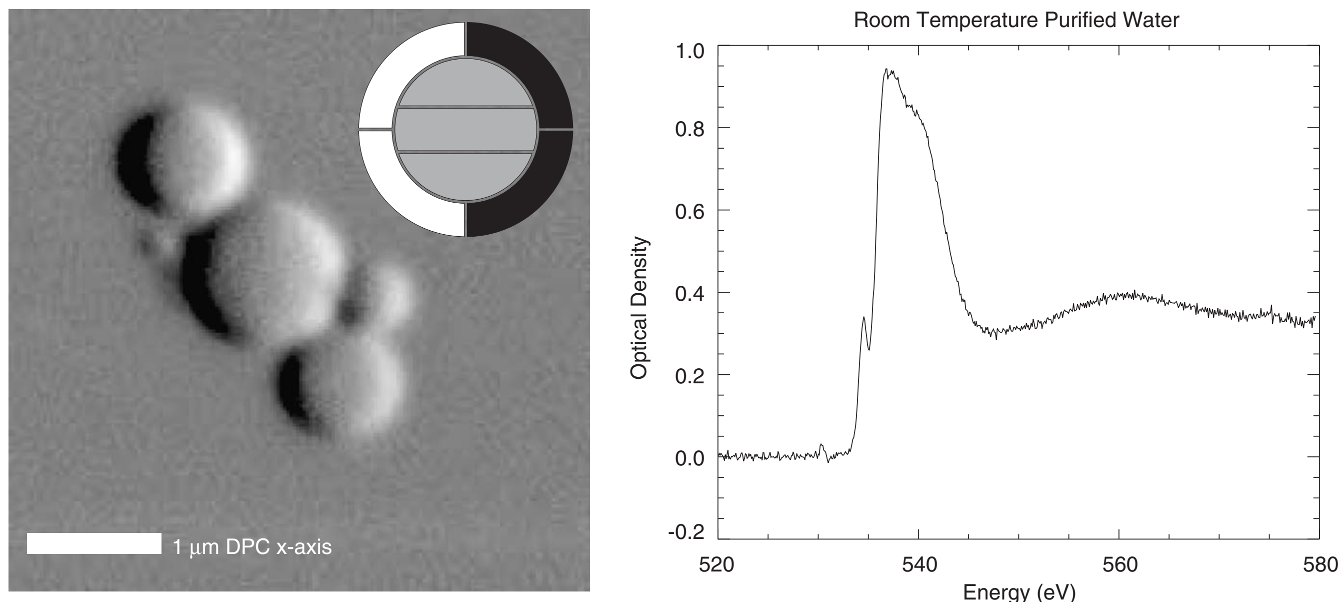

Fig. 14. (Left) Differential phase contrast image of silica spheres recorded at 520 eV photon energy. The image was obtained by subtracting the signal of the two right quadrant segments from the two left quadrant segments. (Right) Point spectrum of purified water obtained at the Oxygen absorption edge. For this data acquisition mode, the sample is held fixed in the focus position and the X-ray monochromator is scanned through the desired energy range.

Advanced Photon Source. Note, however, that a limitation is given by the sharp decrease of quantum efficiency in the detector chip due to the increased absorption length in Silicon above 8 keV (see Fig. 3).

Acknowledgments

The work at Stony Brook University was supported by the National Institutes of Health under Grant R01

EB00479-01A1 and the National Science Foundation under Grant NSF CHE-0221934. Use of the National Synchrotron Light Source and work at the Instrumentation Division at Brookhaven National Laboratory was supported by the US Department of Energy, Office of Science, Office of Basic Energy Sciences, under Contract No. DE-AC02-98CH10886. Work at the MPI-HLL was supported by the Max-Planck-Society.

Appendix A. Noise analysis: further details

The noise analysis for all noise sources involving a $1/f$ power spectrum can be carried out in the time domain. The $1/f$ noise source can be represented by a superposition of randomly arriving pulses $v(t)$. The Fourier representation $V(f)$ of the signal $v(t)$ characterized by the bilateral power spectral density B_f/f can be written as

$$V(f) = \begin{cases} \sqrt{\dfrac{B_f}{2|f|}}(1+j), & f>0 \\ \sqrt{\dfrac{B_f}{2|f|}}(1-j), & f<0 \end{cases} \tag{A.1}$$

which satisfies the condition $V(-f) = V^*(f)$ for $v(t)$ to be real (* indicates the complex conjugate) and the condition $|V(f)|^2 = B_f/f$. The Fourier transform of the real part of $V(f)$ gives the even part $v_e(t)$ of $v(t)$ which is

$$\begin{aligned} v_e(t) &= \int_{-\infty}^{\infty} \mathrm{Re}\{V(f)\}\exp(j2\pi ft)\,df \\ &= \sqrt{2B_f}\int_0^{\infty} \frac{1}{\sqrt{f}}\cos(2\pi ft)\,df \end{aligned} \tag{A.2}$$

where the relation $\exp(j\alpha) = \cos(\alpha) + j\sin(\alpha)$ was used. Evaluating for $t>0$ and substituting $\sqrt{2\pi ft} = \eta$ results in

$$v_e(t) = \begin{cases} 2\sqrt{\dfrac{B_f}{\pi t}}\int_0^{\infty}\cos(\eta^2)\,d\eta \\ \quad = \sqrt{\dfrac{2B_f}{t}}[\mathrm{FresnelC}(\eta)]_0^{\infty} \\ \quad = \sqrt{\dfrac{B_f}{2t}}, & t>0 \\ \quad = \sqrt{\dfrac{B_f}{-2t}}, & t<0 \end{cases} \tag{A.3}$$

where FresnelC(α) is the Fresnel cosine integral. The Fourier transform of the imaginary part of $V(f)$ gives the odd part $v_o(t)$ of $v(t)$:

$$\begin{aligned} v_o(t) &= j\int_{-\infty}^{\infty} \mathrm{Im}\{V(f)\}\exp(j2\pi ft)\,df \\ &= \sqrt{2B_f}\int_0^{\infty} \frac{1}{\sqrt{f}}\sin(2\pi ft)\,df. \end{aligned} \tag{A.4}$$

Again evaluating for $t>0$ and substituting $\sqrt{2\pi ft} = \eta$ gives

$$v_o(t) = \begin{cases} 2\sqrt{\dfrac{B_f}{\pi t}}\int_0^{\infty}\sin(\eta^2)\,d\eta \\ \quad = \sqrt{\dfrac{2B_f}{t}}[\mathrm{FresnelS}(\eta)]_0^{\infty} \\ \quad = \sqrt{\dfrac{B_f}{2t}}, & t>0 \\ \quad = -\sqrt{\dfrac{B_f}{-2t}}, & t<0 \end{cases} \tag{A.5}$$

where FresnelS(α) is the Fresnel sine integral. It follows for the function $v(t)$ that

$$v(t) = v_e(t) + v_o(t) = \Phi(t)\sqrt{\frac{2B_f}{t}} \tag{A.6}$$

where $\Phi(t)$ is the step function. The noise with bilateral power spectral density B_f/f (unilateral $A_f/f = 2B_f/f$) can be represented as a superposition of randomly arriving $\Phi(t)\sqrt{2/t}$ pulses $v(t)$ at rate $B_f = A_f/2$.

References

[1] M. Feser, M. Carlucci-Dayton, C.J. Jacobsen, J. Kirz, U. Neuhäusler, G. Smith, B. Yu, Applications and instrumentation advances with the Stony Brook scanning transmission X-ray microscope, in: I. McNulty (Ed.), X-ray Microfocusing: Applications and Techniques, vol. 3449, Society of Photo-Optical Instrumentation Engineers (SPIE), Bellingham, Washington, 1998, pp. 19–29.
[2] H. Rarback, D. Shu, S.C. Feng, H. Ade, J. Kirz, I. McNulty, D.P. Kern, T.H.P. Chang, Y. Vladimirsky, N. Iskander, D. Attwood, K. McQuaid, S. Rothman, Rev. Sci. Instr. 59 (1988) 52.
[3] C. Jacobsen, S. Lindaas, S. Williams, X. Zhang, J. Microscopy 172 (1993) 121.
[4] A.L.D. Kilcoyne, et al., J. Synchrotron Radiat. 10 (2003) 125.
[5] J. Maser, A. Osanna, Y. Wang, C. Jacobsen, J. Kirz, S. Spector, B. Winn, D. Tennant, J. Microscopy 197 (1) (2000) 68.
[6] J.R. Palmer, G.R. Morrison, Rev. Sci. Instr. 63 (1) (1992) 828.
[7] T. Wilson, C. Sheppard, Theory and Practice of Scanning Optical Microscopy, Academic Press, New York, 1984.
[8] G. Schmahl, D. Rudolph, Proposal for a phase contrast X-ray microscope, in: P.C. Cheng, G.J. Jan (Eds.), X-ray Microscopy: Instrumentation and Biological Applications, Springer, Berlin, 1987, pp. 231–238.
[9] G. Schneider, Ultramicroscopy 75 (1998) 85.
[10] G. Schmahl, D. Rudolph, G. Schneider, P. Guttmann, B. Niemann, Optik 97 (1994) 181.
[11] C.J.R. Sheppard, T. Wilson, Optik 73 (1986) 39.
[12] E. Zeitler, M.G.R. Thomson, Optik 31 (1970) 258, 359.
[13] H.N. Chapman, Ultramicroscopy 66 (1996) 153.
[14] G.R. Morrison, A. Gianoncelli, B. Kaulich, D. Bacesu, J. Kovac, A fast-readout CCD system for configured-detector imaging in STXM, IPAP Conference Series 7 (2006) 377–379.
[15] G.R. Morrison, B. Niemann, Differential phase contrast X-ray microscopy, in: J. Thieme, G. Schmahl, E. Umbach, D. Rudolph (Eds.), X-ray Microscopy and Spectromicroscopy, Springer, Berlin, 1998, pp. I-85–I-94.
[16] J.R. Palmer, G.R. Morrison, Differential phase contrast imaging in X-ray microscopy, in: A.G. Michette, G.R. Morrison, C.J. Buckley (Eds.), X-ray Microscopy III, Springer Series in Optical Sciences, vol. 67, Springer, Berlin, 1992, pp. 278–280.
[17] H.N. Chapman, C. Jacobsen, S. Williams, Ultramicroscopy 62 (3) (1996) 191.

[18] G.R. Morrison, Phase contrast and darkfield imaging in X-ray microscopy, in: C. Jacobsen, J. Trebes (Eds.), Soft X-ray Microscopy, vol. 1741, Society of Photo-Optical Instrumentation Engineers (SPIE), Bellingham, Washington, 1992, pp. 186–193.

[19] S. Vogt, H.N. Chapman, C. Jacobsen, R. Medenwaldt, Ultramicroscopy 87 (2001) 25.

[20] M. Feser, Scanning transmission X-ray microscopy with a segmented detector, Ph.D. Thesis, Department of Physics and Astronomy, Stony Brook University, 2002.

[21] B.L. Henke, E.M. Gullikson, J.C. Davis, Atom. Data Nucl. Data Tables 54 (1993) 181.

[22] L. Strüder, et al., Astron. Astrophys. 365 (2001) L18.

[23] P. Horowitz, W. Hill, The Art of Electronics, second ed., Cambridge University Press, New York, USA, 1989, pp. 220–224.

[24] D.F. Stout, M. Kaufman, Handbook Of Operational Amplifier Circuit Design, McGraw-Hill, New York, NY, USA, 1976, pp. 10.1–10.3

[25] E. Gatti, P.F. Manfredi, Il Nuovo Cimento 9 (1986) 1.

[26] E. Gatti, P.F. Manfredi, M. Sampietro, V. Speziali, Nucl. Instr. and Meth. A 297 (1990) 467.

[27] V. Radeka, Ann. Rev. Nucl. Part. Sci. 38 (1988) 217.

[28] A. Papoulis, Probability, Random Variables, and Stochastic Processes, McGraw-Hill, New York, 1991.

[29] A. Pullia, S. Riboldi, IEEE Trans. Nucl. Sci. NS-51 (4) (2004) 1817.

[30] V. Radeka, $1/f$ noise in physical measurements, IEEE Trans. Nucl. Sci. NS-16 (1969).

[31] E.M. Gullikson, R. Korde, L.R. Canfield, R.E. Vest, J. Electron Spectrosc. Relat. Phenom. 80 (1996) 313.

[32] R. Korde, J.S. Cable, L. Randall Canfield, IEEE Trans. Nucl. Sci. NS-40 (6) (1993) 1655.

[33] B.C. McCallum, M.N. Landauer, J.M. Rodenburg, Optik 101 (2) (1995) 53.

[34] B.C. McCallum, M.N. Landauer, J.M. Rodenburg, Optik 103 (3) (1996) 131.